UC Berkeley
UC Berkeley Previously Published Works

Title
Temperature dependence of secondary electron emission: A new route to nanoscale temperature measurement using scanning electron microscopy

Permalink
https://escholarship.org/uc/item/7v61j9j3

Journal
Journal of Applied Physics, 124(19)

ISSN
0021-8979

Authors
Khan, MI
Lubner, SD
Ogletree, DF
et al.

Publication Date
2018-11-21

DOI
10.1063/1.5050250

Peer reviewed

eScholarship.org
Powered by the California Digital Library
University of California

Journal of Applied Physics

Temperature dependence of secondary electron emission: A new route to nanoscale temperature measurement using scanning electron microscopy

Cite as: J. Appl. Phys. **124**, 195104 (2018); https://doi.org/10.1063/1.5050250
Submitted: 28 July 2018 . Accepted: 27 October 2018 . Published Online: 19 November 2018

M. I. Khan, S. D. Lubner, D. F. Ogletree, and C. Dames

ARTICLES YOU MAY BE INTERESTED IN

Measuring temperature-dependent thermal diffuse scattering using scanning transmission electron microscopy
Applied Physics Letters **113**, 253101 (2018); https://doi.org/10.1063/1.5066111

Temperature and pressure induced Raman studies of C_{60} oxide
Journal of Applied Physics **124**, 195105 (2018); https://doi.org/10.1063/1.5051396

Thermal diodes, regulators, and switches: Physical mechanisms and potential applications
Applied Physics Reviews **4**, 041304 (2017); https://doi.org/10.1063/1.5001072

Lock-in Amplifiers
... and more, from DC to 600 MHz

© 2018 Author(s).

JOURNAL OF APPLIED PHYSICS **124**, 195104 (2018)

Temperature dependence of secondary electron emission: A new route to nanoscale temperature measurement using scanning electron microscopy

M. I. Khan,[1] S. D. Lubner,[1] D. F. Ogletree,[1] and C. Dames[1,2,a)]
[1]*Lawrence Berkeley National Laboratory, 1 Cyclotron Road, Berkeley, California 94720, USA*
[2]*Department of Mechanical Engineering, University of California, Berkeley, California 94720, USA*

(Received 28 July 2018; accepted 27 October 2018; published online 19 November 2018)

Scanning electron microscopy (SEM) is ubiquitous for imaging but is not generally regarded as a tool for thermal measurements. Here, the temperature dependence of secondary electron (SE) emission from a sample's surface is investigated. Spatially uniform SEM images and the net charge flowing through a sample were recorded at different temperatures to quantify the temperature dependence of SE emission and electron absorption. The measurements also demonstrated charge conservation during thermal cycling by placing the sample inside a Faraday cup to capture the emitted SEs and back-scattered electrons from the sample. The temperature dependence of SE emission was measured for four semiconducting materials (Si, GaP, InP, and GaAs) with response coefficients found to be of magnitudes ~100−1000 ppm/K. The detection limits for temperature changes were no more than ±8 °C for 60 s acquisition time. *Published by AIP Publishing.*
https://doi.org/10.1063/1.5050250

I. INTRODUCTION

With the relentless reduction of device sizes in modern microelectronics, power dissipation per unit area is continually increasing and device failure due to thermal hotspots is becoming more common.[1] It is widely understood that the temperature rise due to heat generation in a small length scale can be much higher than predicted by Fourier's law using bulk properties.[2,3] However, experimentally probing temperature in nanostructures is challenging. Among existing methods, scanning thermal microscopy (SThM) provides high spatial resolution[4] but requires physical contact to the sample and is sensitive to tip geometry. Far-field optical thermoreflectance[5] is contact-free, but its spatial resolution is diffraction-limited to a few hundred nanometers. Scanning electron microscopy (SEM), on the other hand, is routinely used to produce high resolution topographic images but has not been used for thermometry before.

A few experimental efforts to measure temperature using electron microscopy have been reported. Electron energy loss spectroscopy (EELS) and cathodoluminescence spectroscopy (CLS) have been used to measure the temperature of metals[6] and semiconducting materials,[7] respectively. Transmission electron microscope (TEM) diffraction patterns of Si and Ge have shown a temperature response coefficient β of around $10^{-3}\,\mathrm{K}^{-1}$ due to thermal diffuse scattering.[8] Here, we define the temperature coefficient β for any signal I as

$$\beta = \frac{1}{I}\frac{\partial I}{\partial T} \approx \frac{1}{\Delta T}\cdot\frac{\Delta I}{I_{avg}}, \tag{1}$$

where I_{avg} is the baseline signal at a reference temperature and ΔI is the signal change due to a temperature change ΔT. A similar thermal-diffuse scattering mechanism has shown $\beta \sim 10^{-4}\,\mathrm{K}^{-1}$ in the electron backscatter diffraction (EBSD) pattern in an SEM.[9] In contrast to those more specialized imaging modes, SEM using secondary electrons (SEs) is the most commonly used imaging mode but has not previously been applied to measure temperature.

Although not performed in an SEM, several past studies using electron beams have reported small temperature effects on SE yield in Ge,[10] MgO,[11] and four magnetic metals.[12] SE emission from a Ge sample[10] was reported to decrease for a sample temperature rise of 500 °C, yielding a temperature coefficient $\beta \sim -10^{-4}\,\mathrm{K}^{-1}$. Single crystal MgO[11] exhibited 20-25% SE yield reduction for about 740 °C temperature rise, corresponding to $\beta \sim -3\times10^{-4}\,\mathrm{K}^{-1}$. SE emission from several metals was also reported to change non-monotonically upon temperature increases of around 400-500 °C, with the scale of $|\beta|$ around 10^{-3}-$10^{-2}\,\mathrm{K}^{-1}$ due to metal to metal phase changes and magnetic transformation.[12]

Here, we show that temperature-dependent SE yield can be measured inside a standard SEM using its built-in SE detector as well as by direct measurements of the absorbed beam current (BC) with a current amplifier. As additional distinctions from the earlier non-SEM works,[10–12] here, we demonstrate this effect using four semiconductors, namely, Si, GaP, InP, and GaAs, and report thermal cycling and charge conservation studies.

II. SECONDARY ELECTRON EMISSION

Here, we briefly review some key aspects of imaging with SEs.[13–15] Secondary electron emission resulting from the primary electron beam of an SEM is a complex process that depends on incident electron energy and angle, as well as on sample composition and topography, surface (first nm) chemical composition and work function, and electron transport inside the bulk sample over hundreds of nanometers. As the primary beam moves across the sample surface, the intensity, energy spectrum, and angular distribution of the

[a)]Electronic mail: cdames@berkeley.edu

secondary electrons change. SEMs are equipped with one or more detectors to record these signals as a function of beam position, generating images. Image contrast is further complicated by the energy-and-angle dependent detector response and collection efficiency. The secondary electron spectrum is typically, and somewhat arbitrarily, divided into "true" secondary electrons with energies of 50 eV or less, and "backscattered" electrons (BSE) with energies of several kV or more. This division reflects the response of typical SEM detectors. "Backscatter" detectors are typically silicon diodes, which are insensitive to electrons below a few kV due to the diode structures, while "secondary" detectors use scintillator/photo-multiplier assemblies that are optimized for low energy electron detection.

To explore SEM thermometry, here we limit ourselves to samples that do not change phase or composition over the temperature range of interest. In such samples, several material parameters change with temperature which could plausibly contribute to a change in SE emission, such as the work function,[16–18] electronic bandgap,[19] and populations of phonons which can scatter SEs, although identifying and elucidating the specific mechanism(s) is beyond the scope of this study.[20] TEM bright field images[8] and SEM EBSD patterns[9] are also known to depend weakly on temperature due to thermal diffuse scattering (the Debye-Waller effect), which can also be understood as temperature-dependent electron scattering.

One practical issue that must be considered is beam-induced sample contamination. In particular, the incident electron beam and/or secondary electrons can induce chemical reactions in organic contaminants present on the sample surface or in the SEM environment, forming surface films made up of reaction byproducts in beam-exposed areas. Depending on the imaging conditions, these carbon-rich films may either reduce (darker image) or enhance (brighter image) the secondary electron emission, resulting in visible "scan squares" when the SEM magnification is reduced after high resolution imaging. We control for this effect by recording secondary electron emission over several temperature cycles to separate temperature dependent changes from dose-dependent changes resulting from contamination.

III. TEMPERATURE DEPENDENT CHARGE CONSERVATION

We used two basic experimental configurations to measure the temperature effects on SEM signals. All measurements were performed in a Zeiss Gemini Supra 55VP-SEM using a primary beam of 5 kV and ~235 pA. In the setup of Fig. 1(a), the sample is mounted inside an aluminum Faraday cup (FC) using silver epoxy. A ceramic sheet is used for dielectric isolation. Because the sample cannot be imaged directly deep inside the Faraday cup using the SEM's built-in SE detector, we first focus on the top of the Faraday cup and then adjust the beam focus downward to the approximate position of the sample surface, ~2.1 mm below the top of the Faraday cup. After this alignment, the primary beam is scanned over a field of view of around $113 \times 85\,\mu\text{m}^2$ at a scan speed of 1 min per frame. All measured currents reported below correspond to a spatial average over this scan frame. This entire Faraday cup assembly is mounted on top of a Peltier heater for temperature control.

The configuration of Fig. 1(a) allows us to measure both the net sample current (NSC) to ground and the current to the Faraday cup, the latter of which captures nearly all (>99%) of the SE and backscattered electron (BSE) leaving the sample, which we define as the emitted current (EC = SE + BSE). The NSC and EC are each measured with their own current amplifier, and both amplifiers share a common electrical ground with the SEM vacuum chamber. Thus, our measurements of the various beam currents are absolute, unlike the signals from the instrument's built-in SE detectors which depend on the (uncalibrated) electron multiplier gain and the SEM working distance (WD). We also note that in the configuration of Fig. 1(a), some of the BSEs striking the aluminum Faraday cup will create their own secondary and back-scattered electrons, some small fraction of which will return to the sample thereby increasing the sample's measured NSC. We have investigated this possible charge recirculation effect using a separate experiment with a split Faraday cup and similarly studied possible artifacts due to thermal expansion, finding both effects to be minor (see Appendix).

Figures 1(c) and 1(d) show a typical test result for a p-doped (boron) silicon sample. Additional sample details are provided in Table I. The sample was cleaned with acetone, methanol, and isopropyl alcohol (IPA), air dried, and finally plasma cleaned before mounting into the high vacuum (5×10^{-5} Torr) SEM chamber. The temperature was cycled stepwise between 15 and 90 °C, waiting for stability of better than ±2 °C before recording temperature and other SE data [Fig. 1(b), in which the sawtooth lines are only schematic guides to the eye]. Temperature was measured with a fine-gauge (0.003 in. wire diameter) K-type thermocouple attached to the top of the Faraday cup using Loctite epoxy adhesive. We estimate that the sample temperature is within 0.1 K of the measured temperature on top of the Faraday cup (Appendix D). For each temperature step, after the system stabilized (settling time ~3.5 min), the EC and NSC were recorded simultaneously while the primary beam was scanned over the $113 \times 85\,\mu\text{m}^2$ field of view through the Faraday cup hole. The EC and NSC were each measured with their own preamplifiers (Femto DLPCA 200, low-pass filtered with 10 Hz cutoff) which were logged via a Keithley 2700 multimeter for the ~1-min frame scan time. The primary beam was otherwise turned off to minimize surface contamination.

The results for EC, NSC, and total beam current BC (defined as BC = EC + NSC) are given in Figs. 1(c)–1(e). At each temperature point, two consecutive frames were analyzed, and we record the median value of the current observed during each frame. The points in Fig. 1 represent the average of these two medians between the two consecutive frames and the error bars show their standard deviation (which is simply $\sqrt{1/2}$ times their difference). Figure 1(c) shows that the EC changes by around ∓ 5 pA for every temperature step ΔT of ±75 °C. This temperature-correlated sawtooth response is superposed on a slow drift of approximately −0.3 pA/min, which we attribute to gradual accumulation of surface contaminants over the course of the imaging session.

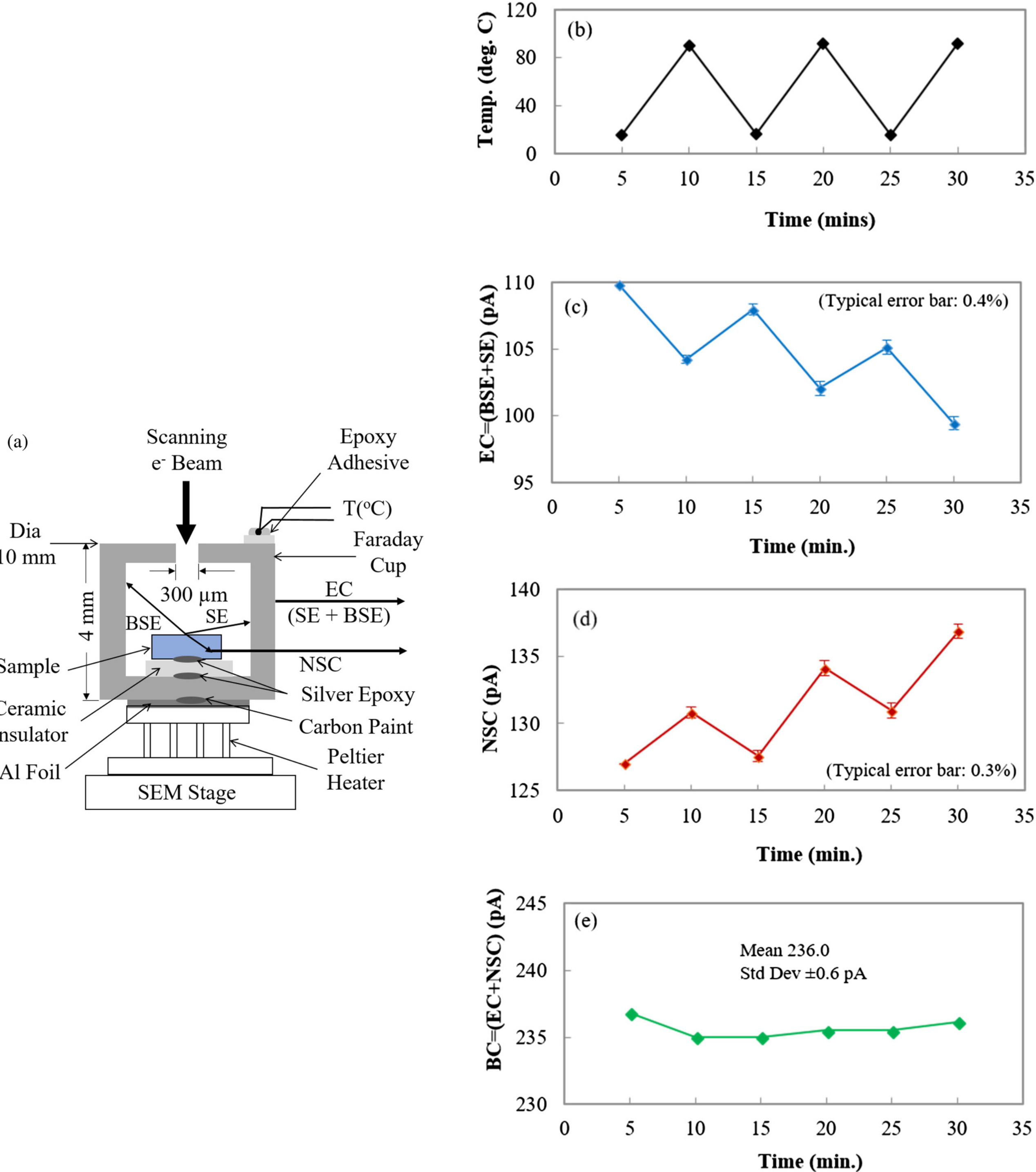

FIG. 1. Test for temperature dependence of charge conservation of a p-type Si sample. Results are averaged over a 1-min scan of a 113×85 (μm)^2 area of the sample's surface. (a) Schematic. (b) Temperature cycling applied by the Peltier stage. (c) Measured current (EC) reaching the Faraday cup, showing a temperature-correlated sawtooth on top of a slow drift. (d) Similar data for the absorbed net sample current (NSC). (e) Sum of EC and NSC demonstrates excellent charge conservation and SEM beam stability. Note that the vertical scales in (c)–(e) all have the same span (15 pA) to facilitate comparisons. The lines in (b)–(e) are schematic guides to the eye.

To isolate the temperature response from this nearly linear drift, we average over the last two complete hot/cold cycles to obtain an average temperature response coefficient $\beta_{EC} = -580$ ppm/K. Similarly, Fig. 1(d) shows that the NSC response is around ±5 pA for ΔT ±75 °C, superposed on a drift of +0.3 pA/min, and after averaging over the last two cycles, we find $\beta_{NSC} = +480$ ppm/K. Importantly, these results show that every change in EC is accompanied by a nearly equal and opposite change in NSC, just as required by charge conservation. To further highlight this charge balance, Fig. 1(e) shows that the sum of the currents from Figs. 1(c) and 1(d) is nearly constant at 236.0 pA, stable to within ±0.6 pA (std. dev.) over this imaging session. Thus, the ∼5 pA steps seen in Figs. 1(c) and 1(d) are statistically significant far above this charge accounting detection limit. In addition to p-type Si, the same charge-accounting setup was also

TABLE I. Tested materials.

Material	Doping type (dopant)	Charge conservation test (EC and NSC) [Fig. 1(a)]	Grayscale imaging test (and NSC) (Fig. 2)	Number of samples tested	Wafer orientation	Doping level (cm^{-3})
Si	Undoped		✓	3	100	…
Si	p-type (B)	✓	✓	6	100	$0.03\text{-}1.7 \times 10^{16}$
Si	n-type (P)		✓	3	100	$8\text{-}9 \times 10^{12}$
GaP	n-type (Si)	✓	✓	2	110	$5\text{-}10 \times 10^{16}$
InP	n-type (Si)		✓	1	110	$5\text{-}10 \times 10^{16}$
GaAs	n-type (Si)		✓	1	110	$5\text{-}10 \times 10^{16}$

applied to study n-type GaP; the β results for both are summarized later in Fig. 4.

IV. TEMPERATURE DEPENDENCE OF SEM GRAYSCALE IMAGE

Having established the basic phenomena using the charge accounting setup of Fig. 1(a), we proceed to a more convenient setup (Fig. 2) which allows for imaging using the SEM's own SE detector. The NSC is also recorded simultaneously as before. The in-lens SE detector was used for recording grayscale images (16 bits), using an incident beam voltage of 5 kV and a typical beam current of 150-260 pA, with the working distance ranging variously from around 3.5-6 mm. In contrast to the configuration of Fig. 1(a), here the sample is placed on top of the Faraday cup. Thus, with the primary beam incident on the sample as shown in Fig. 2, the Faraday cup is simply an electrically conducting link in the circuit for measuring NSC. In addition, the primary beam can be temporarily shifted over to the Faraday cup hole, in which case the wire marked NSC will simply measure the primary beam current (note the gold foil closing the bottom of the cup). For the configuration of Fig. 2, we estimate that the sample temperature is within 1 K of the thermocouple temperature (Appendix D).

Figure 3 shows results from a typical test. An undoped Si sample was thermally cycled between 29 °C and 78 °C, with an uncertainty of ±2 °C. After stabilization at each temperature, three consecutive grayscale images were recorded while simultaneously logging the NSC. Here, the primary beam was kept in continuous averaging mode in between each recording of images. Depending on the sample, the field of view varied from $77 \times 58\,\mu m^2$ to $158 \times 118\,\mu m^2$, with frame acquisition times of around 30 s. For each of the three consecutive images, the median grayscale intensity and NSC were calculated, and each point (error bar) in Figs. 3(b) and 3(c) corresponds to the mean (standard deviation) of those three median values. We were unable to determine the pA-to-grayscale transformation applied by the SEM, so the resulting temperature coefficients of grayscale response are therefore tool- and setting-dependent and only semi-quantitative. For most samples, the SEM's brightness was set to 50% with a few samples at 36-37%, while the contrast was set at 29-36%.

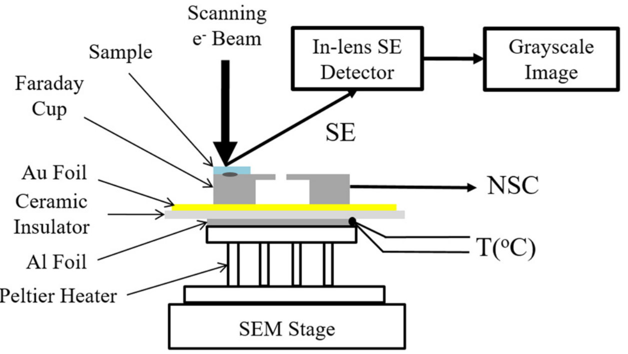

FIG. 2. Schematic of the grayscale test setup. The sample is attached to the top of the Faraday cup using carbon paint, and a metal clip (not shown) presses down the Faraday cup.

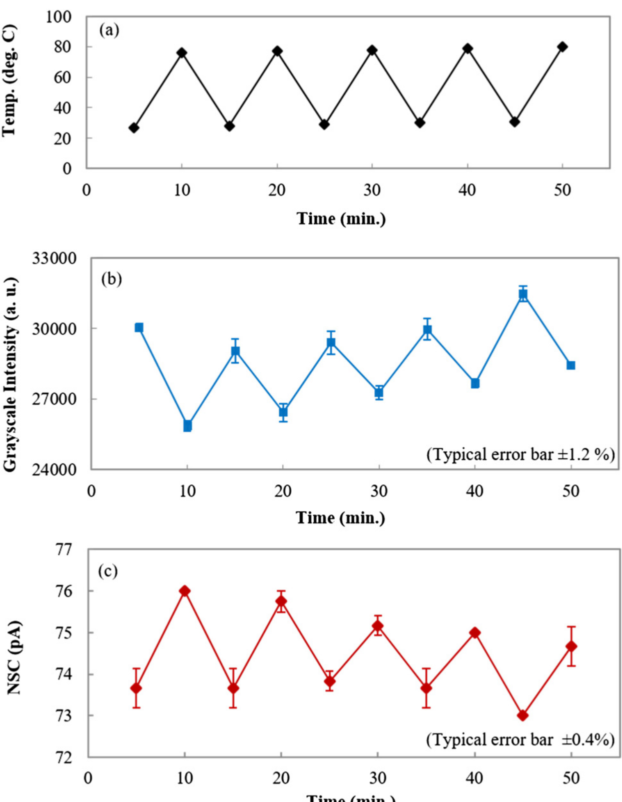

FIG. 3. Typical results for an undoped Si sample using the setup of Fig. 2. (a) Temperature of the sample while being thermally cycled. (b) Thermal response of SEM grayscale intensity using the built-in in-lens SE detector (median grayscale level over the $115 \times 86\,\mu m^2$ field of view). (c) Thermal response of net sample current (NSC), acquired simultaneously with (b). All lines are schematic guides to the eye.

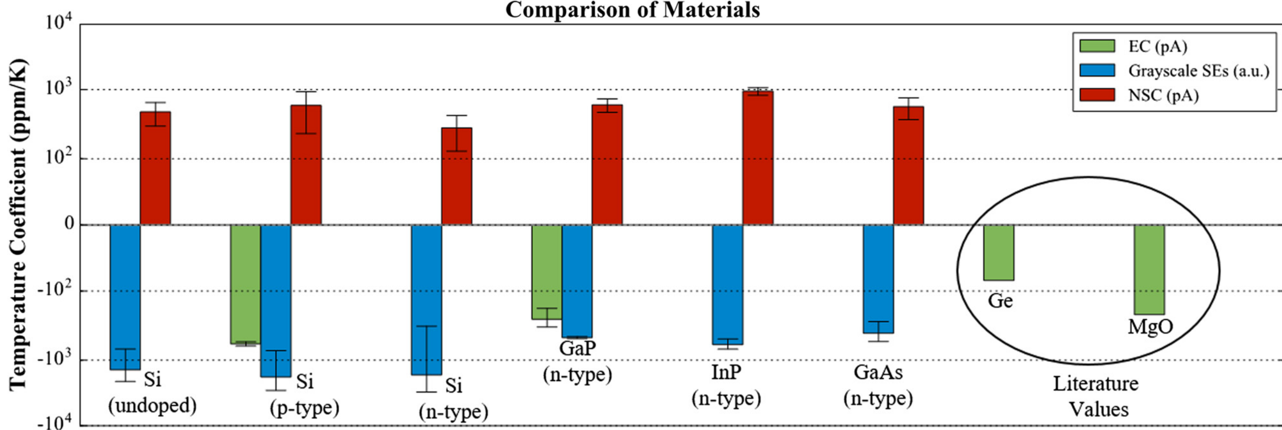

FIG. 4. Summary of thermal response coefficients β of all tested materials. The β axis is logarithmic for both positive and negative values. For sample details, see Table I. Available literature values[10,11] are included for comparison. EC = SE + BSE.

The results for grayscale intensity and net sample current (NSC) are given in Figs. 3(b) and 3(c). Figure 3(b) shows that the mean grayscale intensity changes by around $\mp$3000 a.u. for every temperature step ΔT of $\pm$50 °C, which after averaging over four complete hot/cold cycles corresponds to a temperature response coefficient $\beta_{Grayscale} = -2080$ ppm/K. Similarly, Fig. 3(c) shows that the NSC response is around $\pm$1.8 pA for the same ΔT of $\pm$50 °C, corresponding to $\beta_{NSC} = +490$ ppm/K after averaging. The total primary beam current was separately measured to be around 231.5 pA and was stable within 0.8 pA over the course of the imaging session.

Although the primary beam was left on in between recording images in this test, the surface contamination deposition drift effect is weaker in Figs. 3(b) and 3(c) as compared to the tests of Figs. 1(c) and 1(d). The reasons for this difference are not understood, but we speculate may relate to varying degrees of chamber cleanliness for this shared tool at the start of different imaging sessions, which were spread many days apart.

The main features of Fig. 3 are consistent with those of Fig. 1. In both cases, increasing temperature corresponds to reduced electron yield leaving the sample, whether measured by the SEM's in-lens SE detector [Fig. 3(b)] or the Faraday cup [SE + BSE, Fig. 1(c)]. Furthermore, in both tests increasing temperature corresponds to increasing NSC, as seen in Figs. 1(d) and 3(c).

V. COMPARISON OF TESTED MATERIALS

The measurement techniques described above were applied to the four group III-V and group IV semiconducting materials listed in Table I. Typical sample sizes varied from 3 to 5 mm in each horizontal direction and the thickness was roughly 500 μm. Each sample was cleaned sequentially with acetone, methanol, and IPA and then air dried before mounting in the SEM. Samples used in the charge conservation test were also plasma cleaned as the last step. The measurement results are summarized in Fig. 4, with error bars showing the standard deviation of the temperature response coefficients calculated for each available (cold-hot-cold) thermal cycle, including across multiple samples when available (specified in Table I).

Figure 4 shows that for each tested material, β_{EC} (green bars) and $\beta_{Grayscale}$ (blue) have the same sign and that this is opposite from the sign of β_{NSC} (red), just as expected from considerations of charge conservation. The response coefficients from the in-lens SE detector ($\beta_{Grayscale}$) and the Faraday cup (β_{EC}) can be compared for GaP and p-type Si, with β_{EC} found comparable to but smaller in magnitude than $\beta_{Grayscale}$ in these two cases. Grayscale imaging involves only low energy SEs of ~1-50 eV, while the Faraday cup captures essentially all (>99%) of SEs and BSEs, from 0 eV to 5 keV. Considering these disparate energy scales and the different physical origins of SEs versus BSEs, we consider it unsurprising that temperature could affect the two signals differently. As mentioned above, another important distinction between measurements using the in-lens detector and the Faraday cup is the scaling between pA and grayscale counts, the linearity of which we were unable to confirm with confidence. Although elucidating the physical mechanisms of these response coefficients is beyond the scope of this study, all materials studied have the same qualitative signs of response, namely, increasing temperature tends to reduce the electron emission (negative β_{EC} and/or $\beta_{Grayscale}$) and increase the electron absorption (positive β_{NSC}).

VI. CONSIDERATIONS OF SPATIAL AND TEMPERATURE RESOLUTION

We now briefly consider the temperature detection limits and spatial resolution of the thermometries presented above.

TABLE II. Estimates of the temperature detection limits δT for the four primary results presented above.

Figure	Signal, I	Units of I	β (ppm/K)	$\frac{\delta I}{I}$ (typical) (%)	δT (°C)
1(c)	EC (SE + BSE)	pA	−580	0.4	7
1(d)	NSC	pA	480	0.3	6
3(b)	Grayscale (SE)	a.u.	−2080	1.2	6
3(c)	NSC	pA	490	0.4	8

TABLE III. Grayscale analysis of three subsets of the original $115 \times 86\,\mu m^2$ images used in Fig. 3(b).

Image width (μm)	Image height (μm)	Image area, A (μm^2)	$\beta_{Grayscale}$ (ppm/K)	Averaging time, τ (sec)	Signal uncertainty, $\delta I/I$ (%)	Temperature uncertainty, δT (°C)	Implied noise density, S_N from Eq. (4) (K/$\sqrt{Hz}$)
115	86	9890	−2080	30	1.2	5.6	30
30	30	900	−1930	2.7	1.4	7.0	12
10	10	100	−1880	0.30	1.4	7.3	4.0
1	1	1	−1720	0.0030	1.2	6.8	0.37

For a given uncertainty of the raw signal δI, a simple estimate for the corresponding temperature uncertainty δT is

$$\delta T = \left| \frac{\partial T}{\partial I}\, \delta I \right|.$$

Applying the definition of β from Eq. (1) gives

$$\delta T = \left| \frac{1}{\beta}\, \frac{\delta I}{I} \right|, \tag{2}$$

where values for β and the relative uncertainties $\delta I/I$ (taken here as one standard deviation for simplicity) are available in the results above, summarized in Table II. This calculation shows that in all four cases, the estimated temperature sensitivity is in the range of ±6 °C to ±8 °C. Although this uncertainty is larger than one would like, it should still be relevant for applications like thermal hotspot mapping for device testing and failure analysis, which have temperatures typically reaching 100s of °C above the surrounding ambient.[21,22] It is noteworthy that even though $\beta_{Grayscale}$ is around 5× larger than the other three β's, the uncertainty $[\delta I/I]_{Grayscale}$ is also similarly larger so that the final result for $\delta T_{Grayscale}$ remains consistent with the other three estimates. It must also be noted that the absolute temperature uncertainty for a new, uncalibrated sample is much larger than this detection limit, because of the background drifts and sample-to-sample variability in the $I(T)$ response. See the error bars in the β summary results of Fig. 4.

In conventional SE imaging, longer averaging times τ reduce the noise in a grayscale image, so we investigate the analogous effect on the noise of SE thermal imaging by postulating a noise law like

$$\delta T = \frac{S_N}{\sqrt{\tau}}, \tag{3}$$

where S_N is the spectral noise density in units of K/$\sqrt{Hz}$. Accordingly, we estimate the S_N implied by our measurements as

$$S_N = \delta T \sqrt{\tau}. \tag{4}$$

To check the suitability of Eqs. (3) and (4), we retroactively performed additional analysis on subsets of the gray-scale image data used in Fig. 3(b) (undoped Si, $115 \times 86\,\mu m^2$), by suitably cropping the original images to ~$(30 \times 30\,\mu m^2)$, ~$(10 \times 10\,\mu m^2)$, and ~$(1 \times 1\,\mu m^2)$ fields of view. All cropped frames were located with respect to a unique small sample defect in the original images to avoid artifacts from frame-to-frame image shifts. Just as in Fig. 3(b), for each of these fields of view, we analyzed 3 consecutive frames at each temperature and 5 complete hot-cold cycles, the signal I is the median gray scale counts from a given frame, and δI at each T point is the standard deviation of 3 such I values from the consecutive frames.

The results of this frame-size analysis are given in Table III. In stark contrast to the expected scaling from Eqs. (3) and (4), these results show that δT is nearly independent of the image area size and averaging time, even for this nearly 10 000-fold range of τ. Thus, in these experiments, we see that the uncertainties are not determined by random time-independent noise sources as implicit in Eqs. (3) and (4). We hypothesize instead that δI is dominated by dose-dependent contamination which should scale with the dose in Coulombs per μm^2, though investigating this mechanism, for example, with faster image acquisition times is beyond the scope of this study.

Regarding the potential spatial resolution of SEM thermometry, we first consider the intrinsic physical limits. For thermometry using SEs, we expect that the spatial resolution should be comparable to that of traditional topographical imaging, for which the SEs that can escape the sample emanate from a small volume typically ~5-10 nm in diameter and ~5-50 nm deep.[23] BSEs, on the other hand, scatter throughout a much larger volume of the sample before escaping, typically ~5-10 μm in diameter,[23] which we expect would degrade the spatial resolution of BSE thermometry accordingly. Similarly, because the BSEs impact both EC and NSC signals through charge balance considerations, we expect EC and NSC signals to also have spatial resolution comparable to BSE thermometry and inferior to SE thermometry.

The field-of-view comparison in Table III is consistent with these physical expectations for SE thermometry in that the temperature response is largely independent of the size of the imaging area. The $\beta_{Grayscale}$ value observed for the $1 \times 1\,\mu m^2$ patch is within 17% of that from the original $115 \times 86\,\mu m^2$ image, and as noted above, δT is found to be practically independent of image area even over this nearly 10 000-fold range of areas. We take this as a strong indication that there is no fundamental reason why SE thermometry could not also be practically applied at even smaller length scales.

VII. CONCLUSION

In summary, we have used standard SEM hardware as well as a specialized sample-in-Faraday-cup apparatus to measure the temperature coefficients of electron absorption (β_{NSC}), secondary ($\beta_{Grayscale}$), and secondary + backscatter

(β_{EC}) electron emission of four semiconducting materials. The response coefficients are of magnitudes ~100-1000 ppm/K, which are small enough to go unnoticed in everyday SEM imaging for topography or material composition. On the other hand, these SE and NSC responsivities compare favorably with analogous material response coefficients which are widely exploited for electrical resistance thermometry (typically ~3000-4000 ppm/K for good metals[24]) and optical thermoreflectance (typically ~10-100 ppm/K[25]). It is also confirmed that the SE response coefficient is largely independent of imaging area over the tested range from ~10 000 μm^2 down to 1 μm^2. Thus, we conclude that SEM thermometry has the potential to develop into a practical and widely available tool for non-contact, far-field, thermometry, with possible applications including temperature mapping and thermal property determination.

ACKNOWLEDGMENTS

This work was performed in the Molecular Foundry of the Lawrence Berkeley National Laboratory (LBNL) under user proposal numbers #1623, #2012, #3461, and #3994 and was partially funded by Western Digital Technologies Corporation. The authors thank Ed Wong for technical assistance.

APPENDIX A: LATERAL THERMAL EXPANSION

During thermal cycling, SEM images were observed to move laterally by a few microns due to thermal expansion. For the configuration of Fig. 2, this motion is visible in the raw 2D grayscale map and could be taken into account by using image processing to track the fixed patch of the sample for analysis. Such corrections had only a modest (less than 10%) impact on the calculated temperature response coefficients, $\beta_{Grayscale}$.

For experiments using the charge conservation configuration of Fig. 1(a), there is no such 2D grayscale image available, because by design none of the sample's SEs can escape the Faraday cup to reach the SEM's in-lens detector. To estimate the lateral thermal expansion despite this shortcoming, we performed an auxiliary test. We began by deliberately creating a reference feature on the sample surface which can be detected in the EC and NSC data streams even by the relatively low bandwidth (~10 Hz) picoammeters. We accomplished this by focusing the beam in spot mode on the sample surface for about 3 min to create a localized contamination artifact. As illustrated in Fig. 5, the resulting "bulge" artifact is approximately ~7 μm in diameter and increases the EC by ~2 pA.

Referring to the coordinate system of Fig. 5(a), our SEM rasters quickly along the X direction and slowly along consecutive lines in the Y direction. The picoammeter's limited bandwidth corresponds to an EC time resolution of ~200 ms, which is slow compared to the time for the electron beam to scan a single line (typical frame time 60 s, 768 lines in Y, corresponds to 78 ms per line). Thus, the raw EC data correspond to averaging across all X pixels and around 2.6 lines in Y; that is to say, the EC data in Fig. 5(b) are like a slow 1D scan along Y, with bandwidth limited spatial resolution of ~300 nm (2.6 lines). Similarly, by rotating the scan direction by 90°, the data in Fig. 5(c) represent a slow 1D scan along the sample's X direction.

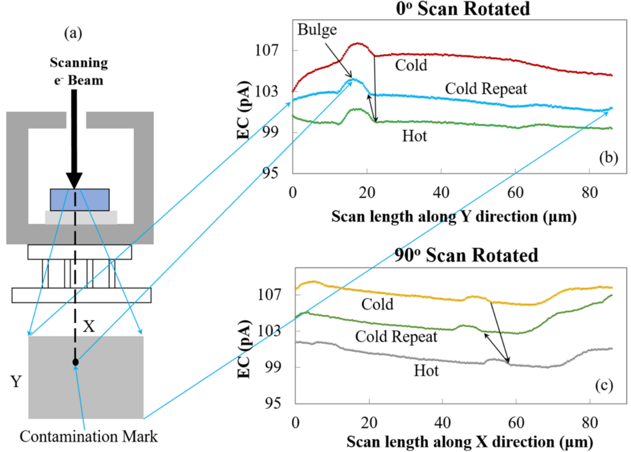

FIG. 5. EC scan profiles for a p-type silicon sample with a "bulge" contamination mark for temperature cycling between 15 °C and 90 °C and two different scan orientations.

With this understanding, we can estimate the in plane thermal expansion from the line scans of Figs. 5(b) and 5(c). First, the EC profiles were recorded at 15 °C (labeled as Cold) for the two orthogonal directions. Then, the sample temperature was raised to 90 °C (labeled as Hot) and the two orthogonal EC traces were repeated. Finally, the sample was returned to room temperature and a third set of orthogonal EC profiles were recorded (Cold Repeat). In all cases, the motion of the contamination "bulge" artifact is readily identified, as shown in Figs. 5(b) and 5(c) with arrows. The corresponding thermal motion is around ~6.4 μm for this 75 K temperature rise. In this setup, the lateral thermal expansion is expected to be dominated by the aluminum Faraday cup [with a coefficient of thermal expansion, (CTE), $= 22 \times 10^{-6}\,K^{-1}$]. Taking the Faraday cup's 5 mm radius as the reference length, a 75 K temperature rise corresponds to around 8 μm of lateral thermal expansion motion, which is reasonably consistent with the ~6.4 μm determined from Fig. 5. Because this thermal motion is small compared to the frame sizes used in the main text, we conclude that any artifacts related to sample motion in and out of the frame are minor. The experiments used to obtain β_{EC} values in the main text were performed on pristine samples without any contamination reference mark.

APPENDIX B: VERTICAL THERMAL EXPANSION AND WORKING DISTANCE CHECK

We also considered the possible impact of vertical thermal expansion, which would shift the sample slightly out of the focal plane of the e-beam. As one way to check this, we recorded EC and NSC for an n-type GaP sample while changing the beam focal plane using the SEM electron optics. The stage itself (physical working distance) was not moved. This test used the sample-in-Faraday-cup configuration of Fig. 1(a).

TABLE IV. Working distance check results.

Imaging sequence	Physical working distance (mm)	Electron optics working distance (mm)	Mean EC (pA)	Mean NSC (pA)
1	5.9	5.9	153 (±2)	71 (±2)
2	5.9	4.9	152 (±2)	72 (±2)
3	5.9	6.9	146 (±2)	79 (±2)

First, with the sample nominally in focus at a working distance (WD) of 5.9 mm, the EC and NSC values were determined (Table IV). The e-beam was blanked except when acquiring EC and NSC values. Then without moving the stage, the e-beam was focused to a working distance of 4.9 mm, with virtually no change seen in the EC and NSC. Then, the electron optics working distance was increased to 6.9 mm, and the mean EC and NSC were found to change by −6 and +7 pA, respectively. We believe this change is caused primarily from the overall drift due to about an hour of imaging in the same area, because these data for the 6.9 mm electron optics working distance were taken at the end of the imaging session. Similar magnitudes and signs of drift over the imaging session are evident in the silicon test presented in Fig. 1. Nevertheless, we can conservatively analyze the results of Table IV by assigning all of the pA changes to working distance effects. Thus, crudely fitting a line to the data in the table, we find the slope of EC versus electron optics working distance is $\frac{\partial(EC)}{\partial(WD)} \approx -3.0\,\mathrm{pA/mm}$. Similarly, $\frac{\partial(NSC)}{\partial(WD)} \approx +3.5\,\mathrm{pA/mm}$.

We can now estimate the magnitude of the corresponding vertical thermal expansion artifact which might corrupt the intrinsic temperature effects on EC and NSC. Taking the Faraday cup's aluminum thickness of $H_o = 0.5$ mm as a reference gauge length, a temperature rise of $\Delta T = 80$ K would cause $\Delta H \approx 0.9\,\mu$m of vertical thermal expansion, equivalent to $\Delta(WD) \approx -0.9\,\mu$m. Thus, using the slopes just estimated from Table IV, the resulting changes in EC and NSC would only be +0.0027 pA and −0.0032 pA, respectively, and thus entirely negligible as compared to the few pA scale of changes reported in Figs. 1 and 3.

APPENDIX C: CHARGE RECIRCULATION TEST

With the sample mounted inside the Faraday cup as in Fig. 1(a), the EC_{Sample} (comprising $SE_{Sample} + BSE_{Sample}$) leaving the sample is collected by the Faraday cup. However, as shown in Fig. 6, from the perspective of the aluminum walls of the Faraday cup, this EC_{Sample} acts like another primary beam, especially the BSE_{Sample} which retains nearly all of its initial 5 kV energy. Thus, EC_{Sample} striking the aluminum Faraday cup will create some additional EC_{Al}, and some fraction of this will return back to the sample. Thus, this charge recirculation effect (similar to a partial reflection from the walls of the Faraday cup) has the potential to increase the apparent NSC_{Sample} and reduce the apparent EC_{Sample}.

To study this additional EC_{Al} effect, we performed a separate experiment using a different sample mounting as shown in the schematics of Fig. 7. We made a modified Faraday cup

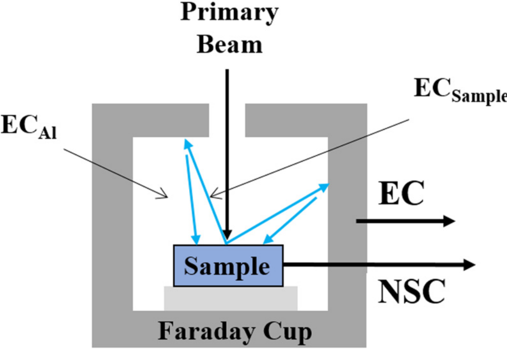

FIG. 6. Schematic of the charge recirculation effect. EC from the sample will cause some additional electrons to be emitted from the aluminum walls of the Faraday cup and some of this EC_{Al} will return to the sample.

(FC), with top and bottom lids electrically isolated by Kapton tape [Fig. 7(b)] and whose bottom lid has a circular opening with diameter 3.7 mm concentric with that of the top lid. This modified Faraday cup is suspended slightly above the sample (p-type Si, size 4.9 mm × 4.1 mm) as shown. The Kapton tape at the bottom of the Faraday cup is used to electrically isolate the Faraday cup from the sample and NSC wire.

The measurements are performed under two configurations. In the "Measurement Closed" (MClosed) configuration shown in Fig. 7(a), the top and bottom lids are electrically connected, while in the "Measurement Split" (MSplit) configuration of Fig. 7(b), the top and bottom lids are electrically distinct and their currents recorded separately. The sample was thermally cycled between 16 °C and 92 °C (beginning with 16 °C) for both configurations.

Figure 8 shows the resulting EC and NSC profiles, while Table V summarizes the mean values of EC and NSC at each temperature. The total ECs from MClosed and MSplit setups were in very close agreement, within around ∼1 pA, as shown in Fig. 8(b). The mean NSCs were also close to each other, being around 2-3 pA less in the MSplit setup [Fig. 8(c)]. In the MClosed setup, the temperature response coefficients for EC and NSC were found from Fig. 8 to be around −590 ppm/K and +380 ppm/K respectively, in reasonably good agreement with the values observed in Figs. 1(c) and 1(d) (−580 ppm/K and +480 ppm/K, respectively). In the MSplit setup, the temperature response coefficients were $\beta_{TL\text{-}EC} \approx -1100$ ppm/K, $\beta_{BL\text{-}EC} \approx -430$ ppm/K, and $\beta_{NSC} \approx +290$ ppm/K.

Finally, to relate these results to the charge recirculation question, note from Figs. 8(a) and 8(b) that roughly equal fractions of EC_{Sample} are absorbed by the top and bottom FC lids, i.e., $EC_{MSplit:BL} \approx EC_{MSplit:TL}$. This means that the BSEs which leave the sample and hit the FC walls are not purely absorbed but also elicit a significant EC_{Al} heading in a downward direction which is ultimately captured by the bottom lid of the FC and/or by the sample. (Of course, multiple such "reflections" among FC surfaces are possible and these experiments can only measure the net effects at top lid and bottom lid.) An important next question is how much of this downward-going EC_{Al} is absorbed by the sample versus by the bottom lid of the FC. Given the broad Lambertian angular distribution of SE and BSE emission,[23] the upward-

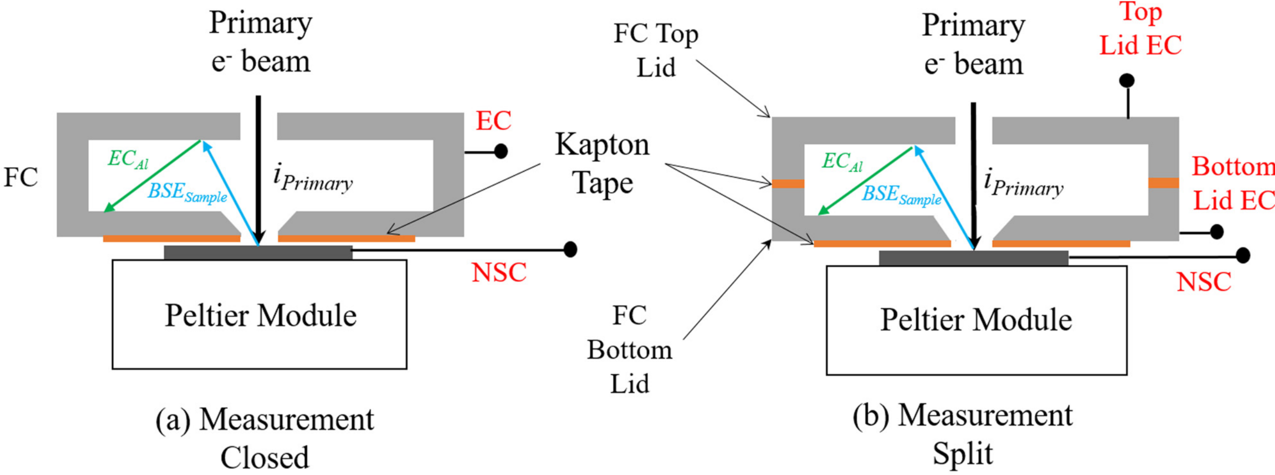

FIG. 7. Modified Faraday cup (FC) setups to study the charge recirculation effect. (a) "Measurement Closed" (MClosed) configuration. (b) "Measurement Split" (MSplit) configuration. Not to scale. Sample is p-type Si.

going EC_{Sample} will irradiate a large area of the FC top lid; and similarly, the subsequently created downward-going EC_{Al} will irradiate an even larger area of the combined (Sample + FC Bottom Lid) zone. Quantitatively, for the experiments of Fig. 1(a), the sample extents in the xy plane (normal to the primary beam) were approximately 4.9 mm × 4.1 mm, whereas in Fig. 7, the bottom lid masked off the sample periphery, leaving exposed the central 3.7 mm

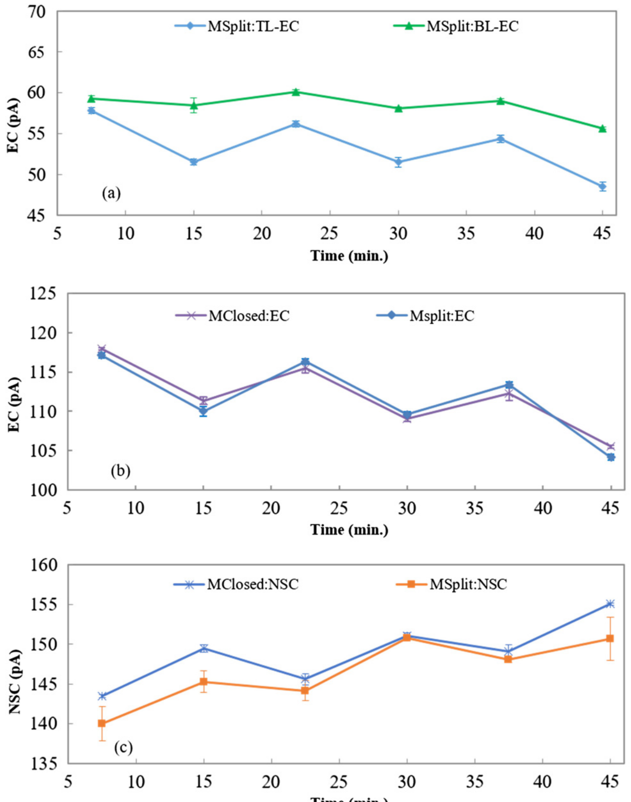

FIG. 8. (a) Measured EC for a p-type silicon sample in the MSplit configuration, which shows that the top lid (TL-EC) and bottom lid (BL-EC) contributions are comparable. (b) Summing these two split lid ECs give the total MSplit:EC, which agrees very closely with the EC measured separately in the MClosed configuration. (c) NSCs for both configurations. In all cases, the sample was cycled between 16 °C and 92 °C, beginning with 16 °C.

(diameter) of the sample. That is, downward-going EC_{Al} in Fig. 1(a) could see 20.1 mm^2 of sample area and thus become NSC, while downward-going EC_{Al} in Fig. 7 can see only 10.8 mm^2 of sample area to become NSC.

For the experiments shown in Fig. 1, the average NSC was 131 pA for a beam current of 236 pA, a ratio of NSC/BC ≈ 0.56. This is consistent for the same material in Fig. 2 configuration as well (summarized in Fig. 4) where the NSC was measured to be 85 pA and the beam current was 157 pA, corresponding to NSC/BC ≈ 0.54. In the setup of Fig. 7, the ratio NSC/BC ≈ 0.57. We see that these results are very similar across the three different setups, essentially within the experimental uncertainty. This means that the fraction of EC_{Al} which strikes the bottom lid of the FC is largely independent of the exposed sample area, within the range of sample area available across the configurations of Figs. 1(a) and 7 (20.1 and 10.8 mm^2, respectively). Considering the large angular spread of EC and fairly small exposed sample area, we conclude that in these presented experiments, the substantial majority of EC_{Al} are likely striking the bottom lid of the FC, not the sample, for both configurations [Figs. 1(a) and 7]. Therefore, we conclude that charge recirculation/reflection artifacts were minor and thus reasonably neglected for the results obtained using Fig. 1(a) configuration of this work, though they certainly could play an important role if the sample area were much larger in the xy plane.

APPENDIX D: ESTIMATION OF SAMPLE TEMPERATURE

For configurations of Figs. 1 and 2, we have estimated the difference between the sample temperature and the

TABLE V. Mean EC and NSC values for MClosed and MSplit setups, at cold and hot states.

	MClosed setup		MSplit setup	
Thermal state	EC (pA)	NSC (pA)	Total EC (pA)	NSC (pA)
Cold (16 °C)	115 (±2.3)	146 (±2.3)	116 (±1.6)	144 (±3.6)
Hot (92 °C)	109 (±2.4)	152 (±2.4)	108 (±2.7)	149 (±3.1)

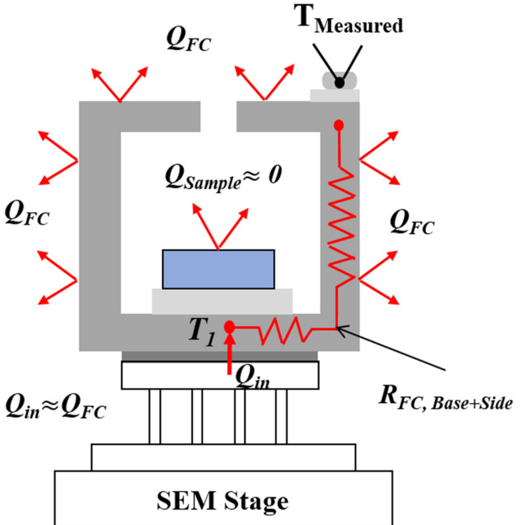

FIG. 9. Schematic of heat dissipation through sample and Faraday cup for Fig. 1 configuration.

temperature measured using the thermocouples attached to the system. For Fig. 1 configuration, the heat dissipation and resistive thermal networks are schematically shown in Fig. 9. The total heat flow through the Faraday cup, Q_{FC}, is estimated to be around 30 mW (assumptions: emissivity of 0.3 for oxidized aluminum, an FC exterior surface area of $2 \times 10^{-4}\,\mathrm{m}^2$, and a temperature difference of 70 K between FC and SEM chamber walls). The indicated conduction resistance of the FC base and side wall is $R_{FC,Base+Side} < 2$ K/W. As a conservative bound, we estimate the temperature difference between point 1 and the thermocouple location by imagining that all of Q_{FC} must flow through this entire $R_{FC,Base+Side}$ path; in reality, some of Q_{FC} is emitted by the FC sidewalls before reaching the top surface where the thermocouple is located. With this conservative treatment, $T_1\text{-}T_{Measured} = Q_{FC} \times R_{FC,Base+Side} < 0.06$ K. Thus, the FC is essentially isothermal to better than 0.06 K. This also means that the net heat flow through the sample is negligible since it is almost completely enclosed within the (nearly) isothermal FC, and so we approximate $T_{Sample} \approx T_1$. Thus, we conclude that the errors between T_{Sample} and $T_{Measured}$ are <0.1 K.

We apply a similar analysis to the experimental configuration of Fig. 2, as indicated in Fig. 10. Now, the

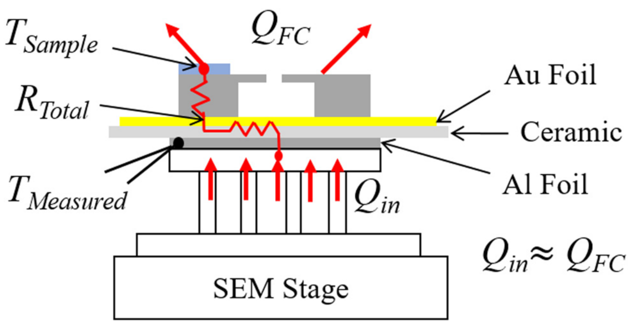

FIG. 10. Schematic of heat dissipation through sample and Faraday cup for Fig. 2 configuration.

estimated Q_{FC} is below 8 mW because this FC has a smaller surface area of $7.5 \times 10^{-5}\,\mathrm{m}^2$ and only 50 K of temperature rise compared to the SEM chamber walls. Again, a conservative estimate of the temperature drop between $T_{measured}$ and T_{sample} assumes that all of this Q_{FC} traverses the path labeled R_{Total} in Fig. 10. We make reasonable estimates for the various contributions to R_{Total}, including a textbook value[26] ($5 \times 10^{-4}\,\mathrm{m}^2\mathrm{K/W}$, corresponding to a vacuum condition at low contact pressure) for the contact resistances at the metal-foil-filled interfaces between the Peltier stage and ceramic plate and between the ceramic plate and FC base. Perfect contact is assumed between the sample and FC top because it was attached with carbon paint. The result is $R_{total} \approx 40\,\mathrm{K/W}$. Thus, the conservative estimate for Fig. 9 is $T_{measured} - T_{sample} < Q_{FC}R_{total} \approx 0.3$ K. Thus, for both configurations of Figs. 1 and 2, the difference between the measured thermocouple temperature and the sample temperature is less than 1 K.

[1]E. Pop and K. E. Goodson, "Thermal phenomena in nanoscale transistors," J. Electron. Packag **128**(2), 102–108 (2006).
[2]G. Chen, "Nonlocal and nonequilibrium heat conduction in the vicinity of nanoparticles," J. Heat Transfer **118**, 539–545 (1996).
[3]P. G. Sverdrup, S. Sinha, M. Asheghi, S. Uma, and K. E. Goodson, "Measurement of ballistic phonon heat conduction near hot spots in silicon," Appl. Phys. Lett. **78**, 3331–3333 (2001).
[4]K. Kim, W. Jeong, W. Lee, and P. Reddy, "Ultra-high vacuum scanning thermal microscopy for nanometer resolution quantitative thermometry," ACS Nano **6**(5), 4248–4257 (2012).
[5]A. J. Schmidt, X. Chen, and G. Chen, "Pulse accumulation, radial heat conduction, and anisotropic thermal conductivity in pump-probe transient thermoreflectance," Rev. Sci. Instrum. **79**, 114902 (2008).
[6]M. Mecklenburg, W. A. Hubbard, E. R. White, R. Dhall, S. B. Cronin, S. Aloni, and B. C. Regan, "Nanoscale temperature mapping in operating microelectronic devices," Science **347**, 629–632 (2015).
[7]M. A. Caldwell, B. Haynor, S. Aloni, D. F. Ogletree, H. S. P. Wong, J. J. Urban, and D. J. Milliron, "Spectroscopic evidence for exceptional thermal contribution to electron beam-induced fragmentation," J. Phys. Chem. C **114**, 22064–22068 (2010).
[8]L. He and R. Hull, "Quantification of electron–phonon scattering for determination of temperature variations at high spatial resolution in the transmission electron microscope," Nanotechnology **23**, 205705 (2012).
[9]X. Wu and R. Hull, "A novel nano-scale non-contact temperature measurement technique for crystalline materials," Nanotechnology **23**, 465707 (2012).
[10]J. B. Johnson and K. G. Mckay, "Secondary electron emission from germanium," Phys. Rev. **93**, 668–672 (1954).
[11]J. B. Johnson and K. G. Mckay, "Secondary electron emission of crystalline MgO," Phys. Rev. **91**, 582–587 (1953).
[12]D. E. Wooldridge, "Temperature effects in secondary emission," Phys. Rev. **58**, 316–321 (1940).
[13]W. S. M. Werner, "Electron transport in solids for quantitative surface analysis," Surf. Interface Anal. **31**, 141–176 (2001).
[14]M. T. Postek and A. E. Vladár, "Modeling for accurate dimensional scanning electron microscope metrology: Then and now," Scanning **33**, 111–125 (2011).
[15]E. Kieft and E. Bosch, "Refinement of Monte Carlo simulations of electron–specimen interaction in low-voltage SEM," J. Phys. D: Appl. Phys. **41**, 215310 (2008).
[16]T. H. Nguyen and S. K. O'Leary, "The dependence of the Fermi level on temperature, doping concentration, and disorder in disordered semiconductors," J. App. Phys. **88**, 3479–3483 (2000).
[17]A. Y. Cho and J. R. Arthur, "Giant temperature dependence of the work function of GaP," Phys. Rev. Lett. **22**, 1180–1181 (1969).
[18]A. R. Hutson, "Velocity analysis of thermionic emission from single-crystal tungsten," Phys. Rev. **98**(4), 889–901 (1955).

[19]K. P. O'Donnell and X. Chen, "Temperature dependence of semiconductor band gaps," Appl. Phys. Lett. **58**, 2924 (1991).
[20]H. J. Fitting, E. Schreiber, J. C. Kuhr, and A. von Czarnowski, "Attenuation and escape depths of low-energy electron emission," J. Electron Spectrosc. Relat. Phenom. **119**, 35–47 (2001).
[21]D. Pierścińska, "Thermoreflectance spectroscopy: Analysis of thermal processes in semiconductor lasers," J. Phys. D: Appl. Phys. **51**, 013001 (2018).
[22]M. Farzaneh, K. Maize, D. Lüerßen, J. A. Summers, P. M. Mayer, P. E. Raad, K. P. Pipe, A. Shakouri, R. J. Ram, and J. A. Hudgings, "CCD-based thermoreflectance microscopy: Principles and applications," J. Phys. D: Appl. Phys. **42**, 143001 (2009).
[23]J. Goldstein, D. Newbury, D. Joy, C. Lyman, P. Echlin, E. Lifshin, L. Sawyer, and J. Michael, *Scanning Electron Microscopy and X-Ray Microanalysis*, 3rd ed. (Springer, New York, 2003) pp. 81, 84, 92.
[24]S. O. Kasap, *Principles of Electronic Materials and Devices*, 3rd ed. (McGraw-Hill, New York, 2006), p. 129.
[25]Y. Wang, J. Y. Park, Y. K. Koh, and D. G. Cahill, "Thermoreflectance of metal transducers for time-domain thermoreflectance," J. Appl. Phys. **108**, 043507 (2010).
[26]T. L. Bergman, A. S. Lavine, F. P. Incropera, and D. P. Dewitt, *Fundamentals of Heat and Mass Transfer*, 7th ed. (John Wiley & Sons Inc., NJ, 2011), p. 118.